Differential contributions of nonmuscle myosin IIA and IIB to cytokinesis in human immortalized fibroblasts

Kei Yamamoto[a], Kohei Otomo[b], Tomomi Nemoto[b], Seiichiro Ishihara[c], Hisashi Haga[c], Akira Nagasaki[d], Yota Murakami[a,e], Masayuki Takahashi[*a,e]

a. Graduate School of Chemical Sciences and Engineering, Hokkaido University, Sapporo 060-8628, Japan
b. Research Institute for Electronic Science, Hokkaido University, Sapporo 001-0020, Japan
c. Faculty of Advanced Life Science, Hokkaido University, Sapporo 060-0810, Japan
d. Biomedical Research Institute, National Institute of Advanced Industrial Science and Technology (AIST), Tsukuba 305-8562, Japan
e. Department of Chemistry, Faculty of Science, Hokkaido University, Sapporo 060-0810, Japan
*Address correspondence to: Masayuki Takahashi, Ph.D. (takahash@sci.hokudai.ac.jp)

Abbreviations

AFM, atomic force microscopy; F-actin, filamentous actin; KO, knockout; NMHC, nonmuscle myosin heavy chain; NMII, nonmuscle myosin II; NMII-F, nonmuscle myosin II filament; SRRF, super-resolution radial fluctuation; WT, wild-type.

Abstract

Nonmuscle myosin II (NMII) plays an important role in cytokinesis by constricting a contractile ring. However, it is unknown how NMII isoforms contribute to cytokinesis in mammalian cells. Here, we investigated the roles of the two major NMII isoforms, NMIIA and NMIIB, in cytokinesis using a WI-38 VA13 cell line (human immortalized fibroblast). In this cell line, NMIIB tended to localize to the contractile ring more than NMIIA. The expression level of NMIIA affected the localization of NMIIB and vice versa. Most NMIIB accumulated at the cleavage furrow in NMIIA-knockout (KO) cells, and most NMIIA was displaced from this location in exogenous NMIIB-expressing cells, indicating that NMIIB preferentially localizes to the contractile ring. Specific KO of each isoform elicited opposite effects. The rate of furrow ingression was decreased and increased in NMIIA-KO and NMIIB-KO cells, respectively. Meanwhile, the length of NMII-filament stacks in the contractile ring was increased and decreased in NMIIA-KO and NMIIB-KO cells, respectively. Moreover, NMIIA helped to maintain cortical stiffness during cytokinesis. These findings suggest that appropriate level of NMIIA and NMIIB in the contractile ring is important for proper cytokinesis in specific cell types. In addition, two-photon excitation spinning-disk confocal microscopy enabled us to image constriction of the contractile ring in live cells in a three-dimensional manner.

Keywords

Nonmuscle myosin IIA; Nonmuscle myosin IIB; Contractile ring; Cytokinesis; Three-dimensional imaging; Cortical stiffness.

1. Introduction

In most animal cells, substantial morphological changes occur in M phase of the cell cycle, such as cell rounding in metaphase and cleavage furrow ingression in cytokinesis [1,2]. These dramatic morphological changes are mechanically supported by the cytoskeleton [3]. During cytokinesis in animal cells, a contractile ring transiently forms in the equatorial plane and generates contractile force to divide a cell into two daughter cells. This contractile ring is mainly composed of actin filaments and nonmuscle myosin II (NMII) filaments [1,2]. The signaling pathway underlying formation of the contractile ring has been partially resolved. RhoA activation following transport of the RhoGEF ECT2 to the equatorial plane is required for accumulation of actin filaments and NMII filaments and formation of the contractile ring [4]. However, the structure and constriction mechanism of the contractile ring are unclear.

NMII consists of two myosin heavy chains (NMHC-IIs) and two pairs of light chains [5,6]. These subunits form two globular heads, which are involved in actin binding and motor activity, and a long α-helical coiled-coil rod-like tail, which is involved in self-assembly into bipolar filaments. NMII dynamically transitions between monomeric and filamentous states, and this process is spatiotemporally regulated in response to various signals [5,6]. To exhibit contractile functions with actin filaments, NMII molecules must assemble into bipolar filaments. It has been hypothesized that bipolar NMII filaments pull actin filaments attached to the plasma membrane from both sides, similar to the mechanism related to sarcomeres in striated muscle, resulting in furrow ingression [1,2,7].

Mammalian cells express three NMII isoforms, termed NMIIA, NMIIB, and NMIIC, which are homodimeric with respect to their heavy chain subunits (NMHC-IIA, NMHC-IIB, and NMHC-IIC, respectively) [5,6]. *In vitro* studies revealed that the two major isoforms, NMIIA and NMIIB, have different motor properties. NMIIA exhibits higher ATPase and motor activities for translocation of actin filaments than NMIIB, whereas NMIIB exhibits a higher affinity for actin filaments than NMIIA because it has a high duty ratio (the fraction of time that the NMII head spends in the strong actin-binding states during the ATPase cycle) [8,9]. Moreover, knockout (KO) of NMIIA and NMIIB in mice leads to embryonic lethality at different developmental stages, indicating that NMII isoforms have different roles in some cellular dynamics [10,11]. It is reported that NMIIA and NMIIB differentially contribute to stress fiber organization [12-14], epithelial cell adhesion [15], and directed cell migration [16,17]. However, their distinct functions in cytokinesis are unknown.

In this study, we established NMIIA-KO and NMIIB-KO cell lines from human immortalized fibroblasts and compared their phenotypes to elucidate the contributions of NMII isoforms to cytokinesis. Our results indicate that the appropriate localization level of NMIIA and NMIIB in the contractile ring is important for proper furrow ingression and that this level is affected by the expression level of each isoform.

2. Materials and methods

2.1. Cell culture, plasmids, antibodies, and reagents

WI-38 VA13 cells (JCRB9057; SV40-transformed WI-38 human embryonic lung fibroblasts) were obtained from

the Health Science Research Resources Bank (Osaka, Japan). These cells were cultured in MEM-alpha (GIBCO/Life Technologies, Carlsbad, CA) supplemented with 10% fetal bovine serum (FBS), 50 U/mL penicillin, and 50 μg/mL streptomycin at 37°C in a humidified incubator containing 5% CO_2. pEGFP-NMHC-IIA and pEGFP-NMHC-IIB were kind gifts from Dr. Robert S. Adelstein (NIH, Bethesda, MD). pmCherry-NMHC-IIA was constructed as previously described [18]. mApple-lifeact-7 (plasmid no. 54747) was purchased from Addgene (Cambridge, MA). Cells were transfected with plasmids using X-fect Transfection Reagent (Takara Bio USA, Mountain View, CA) in antibiotic-free MEM-alpha supplemented with 10% FBS. Rabbit polyclonal anti-NMHC-IIA and anti-NMHC-IIB antibodies targeting the carboxyl termini of NMHC-IIA and NMHC-IIB, respectively, were used as previously described [19,20]. Alexa Fluor 488-conjugated goat anti-rabbit IgG (H+L) and Cy3-conjugated goat anti-rabbit IgG (H+L) were purchased from Jackson ImmunoResearch Laboratories (West Grove, PA). TRITC-conjugated phalloidin was purchased from Sigma-Aldrich (St. Louis, MO). Alexa Fluor 350-conjugated phalloidin was purchased from Molecular Probes (Eugene, OR). Type-I collagen (Cell matrix I-C) was purchased from Nitta Gelatin (Osaka, Japan).

2.2. CRISPR construct design

Guide RNA sequences targeting exon 2 of the human *MYH9* and *MYH10* genes were selected using the CHOPCHOP tool [21]. The following oligonucleotides were used to insert guide RNAs into the pGedit plasmid [22]: guide RNA targeting exon 2 of human *MYH9*, F: 5'-CACCGCAAAGCCACTCTTGTCGGAGT-3' and R: 5'-TTAAACTCCGACAAGAGTGGCTTTGC-3', and guide RNA targeting exon 2 of human *MYH10*, F: 5'-CACCGTGAAGGATCGCTACTATTCGT-3' and R: 5'-TTAAACGAATAGTAGCGATCCTTCAC-3'. Underlines indicate the 20 bp targeting sequence. Blasticidin S was added to the medium at a concentration of 10 μg/mL at 24 h after transfection and was washed out at 72 h after transfection to screen KO cells. CRISPR clones were cultivated for 2–3 weeks, and then clones with no discernible NMIIA or NMIIB expression were selected. Thereafter, six and seven surviving clones were screened to analyze KO of NMIIA and NMIIB, respectively.

2.3. Immunofluorescence

Cells cultured on coverslips (Matsunami, Kishiwada, Japan) coated with 0.3 mg/mL collagen were fixed with 3.7% formaldehyde prepared in phosphate-buffered saline (PBS) for 15 min and permeabilized with 0.1% Triton X-100 prepared in PBS for 10 min. Fixed cells were incubated with blocking solution (3% bovine serum albumin prepared in PBS) for 15 min. Thereafter, cells were incubated with primary antibodies diluted in blocking solution for 60 min, washed three times with PBS, incubated with the appropriate secondary antibodies diluted in blocking solution for 60 min, and subsequently washed three times with PBS. For indirect immunofluorescence, rabbit polyclonal anti-NMHC-IIA and anti-NMHC-IIB primary antibodies were diluted 1:5,000. Cy3-conjugated goat anti-rabbit IgG (H+L) and Alexa Fluor 488-conjugated goat anti-rabbit IgG (H+L) secondary antibodies were diluted 1:500 and 1:200, respectively. Actin filaments were stained with Alexa Fluor 350-conjugated phalloidin or TRITC-conjugated phalloidin. For direct immunofluorescence, antibodies were labeled with Alexa Fluor 488 or Alexa Fluor 596 using

a Zenon Antibody Labeling kit (Molecular Probes) according to the manufacturer's protocol. Samples were incubated with Alexa Fluor 596-conjugated anti-NMHC-IIA (1:2,000) and Alexa Fluor 488-conjugated anti-NMHC-IIB (1:2,000) antibodies for 60 min. Thereafter, cells were fixed again with 3.7% formaldehyde prepared in PBS for 15 min and incubated with Alexa Fluor 350-conjugated phalloidin for 60 min. Images were acquired using a conventional fluorescence microscope (BX50WI; Olympus, Tokyo, Japan) equipped with a single-chip color CCD camera (DP70; Olympus) and an objective lens (LCPlanFl 20×/0.40 NA or UPlanApo 60×/0.90 NA; Olympus) together with DP Controller software (Olympus). Three-dimensional images were acquired using an inverted microscope (Ti-E; Nikon, Tokyo, Japan) and a confocal laser microscope system (A1R; Nikon) equipped with an oil-immersion objective lens (Plan Apo VC 60×/1.40 NA Oil; Nikon). All images were acquired using NIS-Elements C software (Nikon), and all procedures were performed at room temperature. Immunofluorescence images were analyzed using ImageJ software (NIH).

2.4. Time-lapse observation

Transfected cells were plated onto glass-bottom dishes (Iwaki, Tokyo, Japan) coated with 0.3 mg/mL type-I collagen (Cell matrix I-C; Nitta Gelatin). Two-dimensional time-lapse images were acquired using an inverted microscope (IX71; Olympus) equipped with a single-chip color CCD camera (DP70; Olympus) and an objective lens (UPlanFl 100×/1.30 NA Oil; Olympus). During observation, cells were warmed on a thermoplate set to 37°C (MATS-U55R30; Tokai Hit, Fujinomiya, Japan). Images of rounded cells were acquired every 30 s from anaphase onset using DP Controller software (Olympus).

2.5. Line profile analysis

Line profile analysis was referred to the previous study [23]. Dividing cells with a furrow width less than 10 μm were selected for line profile analysis along the cortex of fixed cells. Chromosomes were visualized using DAPI to confirm cytokinesis. Fluorescence intensities were normalized against the integrated intensity of each line profile (set to 1) after subtraction of cytoplasmic background. All images were analyzed using ImageJ software.

2.6. Two-photon excitation spinning-disk confocal microscopy analysis

The two-photon excitation spinning-disk confocal microscopy system used a femtosecond mode-locked Titanium-Sapphire laser (Mai Tai eHP DeepSee; Spectra Physics, Santa Clara, CA), which generates pulses of light with a wavelength of 920 nm to simultaneously excite mCherry-NMHC-IIA and EGFP-NMHC-IIB. Laser power was adjusted using a variable neutral-density filter. Beam width was increased to ca. ϕ 8 mm by applying a beam expander comprising a pair of plano-convex lenses. This enlarged beam was introduced into a spinning-disk scanner with 100 μm-wide pinholes aligned on a Nipkow disk (CSU-MPϕ100; Yokogawa Electric, Kanazawa, Japan) installed on an inverted microscope (Ti-E; Nikon) with a stage incubator set to 37°C and containing 5% CO_2 (INUG2-TIZB; Tokai Hit). The incident excitation light was introduced at the pupil of the objective lens (CFI Plan Apo IR 60XWI 60×/1.27

NA; Nikon) and focused on multiple points of a specimen. Fluorescent signals acquired by the objective lens were passed through the Nipkow disk, reflected by the first dichroic mirror (700–1,100 nm bandpass; Yokogawa Electric), passed through two infrared ray cut filters (FF01-770/SP-25 × 2; Semrock, Rochester, NY), separated into one pair of dual wavelength images using image-splitting optics (W-View Gemini; Hamamatsu Photonics, Hamamatsu, Japan) including a second dichroic mirror (FF580-FDi01-25x36; Semrock) and bandpass filters (FF01-528/38; Semrock and 630/60; Nikon), and finally focused on an EM-CCD camera (iXon Ultra 897; Andor Technology, Belfast, UK) using relay lenses with a magnification of ×1.2. Z-scans were performed with a piezo actuator (P-721; Physik Instrumente, Karlsruhe, Germany). All images were acquired using NIS-Elements C software (Nikon).

2.7. Super-resolution radial fluctuation (SRRF) analysis

Immunofluorescence was performed as described above. Rabbit polyclonal anti-NMHC-IIA and anti-NMHC-IIB primary antibodies were diluted 1:1,000. The Alexa Fluor 488-conjugated goat anti-rabbit IgG (H+L) secondary antibody was diluted 1:200. Fixed samples were mounted onto slide glasses using 10 μL of SlowFade Diamond Antifade Mountant (Thermo Fisher Scientific, Waltham, MA). Raw images were acquired using the confocal laser scanning microscope system described above and NIS-Elements C software (Nikon). These images were processed using super-resolution radial fluctuation (SRRF) with parameters recommended by the ImageJ plugin [24]. For quantification of the lengths of NMII-filament (NMII-F) stacks, regions measuring 6×6 μm^2 and 4×4 μm^2 at the equatorial plane were selected to analyze the early and middle stages of furrow ingression, respectively. Stack length was defined as the length of the long axis of each fluorescent signal after ellipse approximation using ImageJ software.

2.8. Atomic force microscopy (AFM)

Atomic force microscopy (AFM) indentations to measure cortical stiffness were performed using a Nanowizard 4 (JPK Instruments, Berlin, Germany) mounted on a TE300 microscope (Nikon). Pyramidal silicon nitride cantilevers (MLCT; Veeco, Woodbury, NY) with a spring constant of 0.06 N/m were used. The spring constant of the cantilevers was calibrated by thermal tuning using the simple harmonic oscillator model. Samples were indented with a calibrated force of 1.5 nN in a scan area of 0.25 μm^2 (four pixels × four lines). The Hertz model of impact was used to determine the elastic properties (Young's modulus). A Poisson's ratio of 0.5 was used to calculate Young's modulus.

3. Results

3.1. NMIIB is more concentrated in the cleavage furrow than NMIIA during cytokinesis

NMIIA and NMIIB both localize to the cleavage furrow in HeLa cells during cytokinesis [25]. However, the relative level of localization of each isoform to the contractile ring is unclear. In this study, we used WI-38 VA13 cells (hereafter referred to as VA13 cells) because they exhibited typical shape changes during M phase (cell rounding and cleavage furrow ingression) and expressed both NMIIA and NMIIB (Fig. S1A). We roughly estimated that the expression level of NMHC-IIA was about 7.5-fold higher than that of NMHC-IIB in VA13 cells (Fig. S1B and C).

The expression level of NMHC-IIC was below the detection limit of immunoblotting in these cells (Fig. S1A). To examine the localizations of NMIIA and NMIIB in VA13 cells during cytokinesis, we performed immunofluorescence staining of endogenous NMHC-IIA and NMHC-IIB together with visualization of actin filaments. Immunofluorescence images and line profile analysis along the cell cortex revealed that NMIIA and NMIIB were both enriched in the cleavage furrow at the onset of furrow ingression (Fig. 1A and B). Moreover, immunofluorescence images showed that NMIIB was more enriched in the equatorial region than NMIIA at this stage (Fig. 1A). As ingression progressed, both isoforms became concentrated at the cell cortex. In particular, NMIIB was distributed less in the cytoplasm and was enriched in the cleavage furrow (Fig. 1A and B). These results illustrate that NMIIB tends to localize to the contractile ring more than NMIIA. Next, we performed immunofluorescence staining of endogenous NMHC-IIA and NMHC-IIB followed by conventional confocal microscopy to acquire images showing the three-dimensional localizations of NMIIA and NMIIB during cytokinesis. NMIIB was enriched in the equatorial region on the basal side during the early stage of cytokinesis, and both isoforms, especially NMIIB, accumulated in the contractile ring (Fig. 1C and D).

3.2. Three-dimensional time-lapse imaging of formation and constriction of the contractile ring

Next, we attempted to acquire three-dimensional time-lapse images of the formation and constriction of the contractile ring. It is difficult to perform whole cell imaging of these processes in a three-dimensional manner in living mammalian cells because they occur rapidly and cells are rounded and thus thick. To acquire three-dimensional time-lapse images of these events, we used a two-photon excitation laser scanning microscope equipped with a spinning-disk confocal scanning unit [26,27]. This system provides benefits in terms of less invasive excitation only to the focal plane and involves high-speed scanning by a spinning disk, allowing three-dimensional time-lapse imaging of microtubule dynamics during cytokinesis in live plant cells [27]. In addition, a single wavelength of the two-photon excitation laser light excites fluorochromes over a wide range of excitation wavelengths [28], enabling simultaneous acquisition of dual wavelength images using image-splitting optics [27]. Thus, we expected this system to enable us to image formation and constriction of the contractile ring in live animal cells in a three-dimensional manner. We performed this imaging using VA13 cells exogenously expressing mCherry-NMHC-IIA and EGFP-NMHC-IIB. Both isoforms were distributed throughout the cell cortex at the rounding stage and accumulated at the contractile ring during furrowing (Fig. 2A and Movie S1). We successfully observed constriction of the contractile ring as a circular shape in a three-dimensional manner using this microscopic system (Fig. 2B).

3.3. The expression levels of NMIIA and NMIIB affect their localizations to the cleavage furrow

To investigate the individual contribution of each NMII isoform to cytokinesis, we generated NMIIA-KO and NMIIB-KO cells using the CRISPR/Cas9 system and analyzed their phenotypes. Specific KO of each isoform was confirmed by immunoblotting and immunofluorescence analyses (Fig. S2A and C). The expression level of the remaining NMII isoform was not markedly changed (Fig. S2A and B). Clones A1 and B1 were mainly used as

NMIIA-KO and NMIIB-KO cells in further analyses, respectively.

Immunofluorescence staining revealed that localization of NMIIB to the cleavage furrow was markedly higher in NMIIA-KO cells than in wild-type (WT) cells (Fig. 3A and C); however, localization of NMIIA to the cleavage furrow was only slightly higher in NMIIB-KO cells than in WT cells (Fig. 3B and D). These results indicate that the remaining NMII isoform in NMIIA-KO and NMIIB-KO cells localizes to the cleavage furrow more than in WT cells, probably to compensate for loss of the other NMII isoform. They also suggest that the amount of NMIIA is higher than that of NMIIB at the cleavage furrow in VA13 cells. Most molecules of NMIIB, whose expression level was much lower than that of NMIIA, likely accumulated at the cleavage furrow in NMIIA-KO cells to compensate for the absence of NMIIA, which was the major isoform present at this location in WT cells.

Next, we investigated the effects of exogenous expression of each NMII isoform on the localizations of endogenous NMII isoforms. Exogenous expression of EGFP-NMHC-IIB suppressed accumulation of NMIIA at the cleavage furrow, whereas exogenous expression of EGFP-NMHC-IIA affected accumulation of NMIIB to a lesser extent (Fig. S3). These results suggest that a limited number of NMII molecules can localize to the cleavage furrow and that NMIIB preferentially accumulates at this location. This is probably because the assembly ability of NMIIB is greater than that of NMIIA (this is discussed further in the Discussion section). Taken together, the localizations of NMIIA and NMIIB to the cleavage furrow are regulated by the delicate balance of their relative expression levels and their molecular properties.

3.4. An appropriate level of NMIIA and NMIIB is important for normal organization of NMII-F stacks in the contractile ring

NMII-F stack, which is an arrayed structure consisting of multiple bipolar NMII filaments, was previously detected in lamella of fibroblasts by electron microscopy and suggested to be important for formation of actin filament bundles in this region [29]. Super-resolution imaging modalities, such as structured illumination microscopy (SIM), revealed the dynamic organization of NMII-F stacks, which are generated at the distal region of lamella and expanded during their inward flow [30-33]. NMII-F stacks were also previously observed in the cleavage furrow by SIM and suggested to contribute to proper orientation of actin filaments and generation of a larger contractile force in the contractile ring [30,33]. Treatment with a low concentration of blebbistatin, an inhibitor of NMII ATPase activity, shortens NMII-F stacks and decelerates furrow ingression [30], suggesting that proper organization of NMII-F stacks correlates with proper progression of furrow ingression. Here, we attempted to examine the organization of NMII-F stacks in the contractile ring of NMIIA-KO and NMIIB-KO cells using SRRF, which is a newly developed method for super-resolution imaging that only requires a conventional confocal microscope [24]. In this experiment, we focused on the organization of stacks located at the bottom of the cleavage furrow (Fig. 4A) because the relatively flat plane of this region was advantageous for SRRF analysis. The mean length of NMII-F stacks detected using an anti-NMHC-IIA or anti-NMHC-IIB antibody increased with the progression of furrow ingression in WT cells (Fig. 4B and C). The mean length of NMII-F stacks at middle stage was comparable in size to that observed by SIM [30,33]. This indicates

that NMII-F stacks contain both NMIIA and NMIIB and that their expansion correlates with the progression of furrow ingression. Next, we measured the length of NMII-F stacks in the contractile ring of NMIIA-KO and NMIIB-KO cells, which consisted of filaments composed of the remaining NMII isoform. In NMIIA-KO cells, the mean length of NMII-F stacks was longer than in WT cells and extremely long stacks were observed (Fig. 4D and F). By contrast, the mean length of NMII-F stacks was shorter in NMIIB-KO cells than in WT cells (Fig. 4E and F). These results suggest that the appropriate localization level of NMIIA and NMIIB is important for proper organization of NMII-F stacks at the cleavage furrow. Additionally, NMIIB might expand NMII-F stacks.

3.5. NMIIA and NMIIB accelerate and decelerate constriction of the contractile ring, respectively

Next, we performed time-lapse imaging to investigate cytokinesis in NMIIA-KO and NMIIB-KO cells, in which the contractile ring contained the remaining NMII isoform. To clearly observe the cell cortex, we analyzed cells expressing mApple-lifeact, which binds to actin filaments (Movie S2 and Fig. 5A). We tracked changes in the cleavage furrow width over time (Fig. 5B and C). The furrow ingression rate was lower in NMIIA-KO cells (1.40 ± 0.40 μm/min, n=10) than in WT cells (2.07 ± 0.69 μm/min, n=10) (Fig. 5C and D). By contrast, the furrow ingression rate was slightly higher in NMIIB-KO cells (2.46 ± 0.39 μm/min, n=10) than in WT cells, although this difference was not statistically significant. KO of NMIIA and NMIIB had opposite effects on the furrow ingression rate. These results indicate that NMIIB in NMIIA-KO cells and NMIIA in NMIIB-KO cells decrease and increase the furrow ingression rate, respectively. NMIIA and NMIIB may accelerate and decelerate constriction of the contractile ring, respectively, due to their motor properties [8,9]. KO of NMIIA and NMIIB also elicited opposite effects on NMII-F stack organization (Fig. 4F), suggesting that proper organization of these stacks correlates with the furrow ingression rate.

3.6. NMIIA helps to maintain cortical stiffness during cell division

During time-lapse observation, we noticed that membrane blebbing in polar regions occurred in WT and NMIIB-KO cells, but not in NMIIA-KO cells (Movie S2 and Fig. S4). We hypothesized that KO of NMIIA affects cortical stiffness because blebbistatin blocks blebbing [34] and decreases cortical stiffness in mitotic cells [35,36]. We attempted to directly measure cortical stiffness in rounded mitotic cells by AFM [37] and evaluated the contributions of NMIIA and NMIIB using KO cells. The tip of the cantilever was carefully positioned on top of a rounded cell to measure cortical stiffness (Fig. 6A). Stiffness was significantly lower in NMIIA-KO cells than in WT cells, but was almost the same in NMIIB-KO and WT cells (Fig. 6B). NMIIB-KO and WT cells exhibited inter-individual variation in stiffness. It was recently demonstrated that cortical stiffness markedly changes during cell division; it significantly increases during anaphase and telophase, which is most likely due to an increase in cortical tension [37]. In this study, we were unable to reliably distinguish between cells in which anaphase had begun and thus in which it had not. This may explain the variation in stiffness observed in WT and NMIIB-KO cells. By contrast, stiffness varied little in NMIIA-KO cells, indicating that it did not differ before and after anaphase onset; specifically, stiffness remained low

in these cells throughout cell division. These results suggest that NMIIA, which localizes to the cell cortex, helps to maintain cortical stiffness during cytokinesis in VA13 cells.

4. Discussion

This study investigated the contributions of NMIIA and NMIIB to cytokinesis. Analyses of isoform-specific KO cells, which were generated from human immortalized fibroblasts, revealed that cytokinesis is controlled by proper organization of the contractile ring, which is dependent on the distinct biochemical properties of NMIIA and NMIIB and their relative level of accumulation to this location.

We showed that NMIIB preferentially accumulated at the cleavage furrow (Fig. 7). Exogenous expression of EGFP-NMHC-IIB displaced endogenous NMIIA from the cleavage furrow (Fig. S3). Even in untreated control cells, the relative accumulation level of NMIIB to the contractile ring was higher than that of NMIIA (Fig. 1). This observation was also made in MRC-5 SV1 TG1 cells (the other type of human immortalized fibroblasts) and HeLa cells (data not shown). Most NMIIB molecules accumulated at the cleavage furrow in NMIIA-KO cells (Fig. 3), whereas a limited number of NMIIB molecules accumulated at this location in WT cells (Fig. 1). Expression of NMHC-IIA was about 7.5-fold higher than that of NMHC-IIB (Fig. S1). We assume that the excessive amount of NMIIA limits the localization of NMIIB to the contractile ring.

The mechanism underlying the distinct localizations of NMII isoforms in migrating cells is suggested to involve dynamic transition between monomeric and filamentous states. Specifically, NMIIA is more dynamic than NMIIB and therefore reaches the anterior region faster than NMIIB [38,39]. The C-terminal tail regions of each NMII isoform, which include the assembly competence domains [40], determine their dynamic properties in cells [38,39]. *In vitro* studies using recombinant C-terminal rod fragments of NMII isoforms revealed that a higher level of NMIIB than NMIIA assembles into filaments under physiological salt conditions [40,41]. This suggests that the dynamic properties of NMII isoforms in cells are dependent on their assembly properties. Thus, NMIIB tends to remain in the posterior region of migrating cells due to its higher assembly ability. It was reported that the C-terminal rod region of NMIIB determines its specific localization to the contractile ring in dividing immature megakaryocytes [42], indicating that the assembly ability of NMIIs is also important for their equatorial localization during cytokinesis. NMIIA and NMIIB were also reported to co-assemble into heterotypic filaments in the contractile ring [43] and stress fibers [43,44]. Moreover, NMIIA was suggested to affect the dynamic transition of NMIIB from heterotypic filaments to the monomeric form in stress fibers [13]. NMIIA may also elicit this effect on NMIIB in the contractile ring.

NMIIB is the only NMII isoform present in the contractile ring in immature megakaryocytes [45]. Thus, the preferential accumulation of NMIIB at the contractile ring in these cells may be an extreme case. Interestingly, NMIIB expression is repressed during differentiation of megakaryocytes, resulting in polyploidization by endomitosis, and NMIIA cannot accumulate at the contractile ring during this physiological event [45]. However, multinucleation was not observed in NMIIA-KO or NMIIB-KO cells (Fig. S2D); the remaining NMII isoform localized to the cleavage furrow and compensated for loss of the other NMII isoform. If there is a gap in the contractile

ring in mitotic cells, NMII molecules can localize there, regardless of the isoform. Taken together, we assume that the total number of NMII molecules in the contractile ring is limited and that the relative level of localization of NMIIA and NMIIB to the contractile ring is delicately regulated by their relative expression levels and assembly abilities.

In addition to their distinct dynamic properties, NMIIA and NMIIB have different motor properties, as characterized by *in vitro* studies [8,9]. Based on these studies, NMIIA and NMIIB were suggested to mainly translocate and crosslink actin filaments, respectively [5,6]. Accordingly, NMIIA and NMIIB help to generate contractile force and maintain stress fibers in the contracted state, respectively [14,46]. In the same manner, NMIIA and NMIIB may translocate and crosslink actin filaments in the contractile ring, respectively (Fig. 7). This hypothesis is supported by the finding that the furrow ingression rate was decreased and increased in NMIIA-KO and NMIIB-KO cells, respectively. Using recombinant full-length NMIIA and NMIIB molecules, the kinetic and mechanical properties of heterotypic filaments *in vitro* were recently shown to differ according to the ratio of these isoforms. Interestingly, the movement rate of NMII filaments on actin filaments is affected by the presence of even a small amount of NMIIB [47]. It was suggested that progressive compaction and organization of contractile ring accelerate furrow ingression, while limitations on contractile ring disassembly decelerate it during cytokinesis [48]. NMIIB may limit the disassembly of contractile ring due to its crosslinking ability for actin filaments.

Super-resolution imaging recently revealed that NMII filaments form in the distal region of lamella and expand into NMII-F stacks during their inward movement in migrating cells [30-33]. Interactions of NMII filaments on actin filaments in transverse arcs are required for expansion of stacks [31,32]. Moreover, NMIIB is incorporated into existing filaments consisting of NMIIA during inward movement, and heterotypic filaments consequently form in the proximal region of lamella [44]. These results led us to speculate that expansion of stacks correlates with the presence of NMIIB. Super-resolution imaging using SRRF revealed that the length of stacks formed in the contractile ring was increased and decreased in NMIIA-KO and NMIIB-KO cells, respectively (Fig. 4). We speculate that an increased amount of NMIIB causes excessive stack expansion in NMIIA-KO cells, while a lack of NMIIB perturbs stack expansion in NMIIB-KO cells. KO of UNC-45a, a molecular chaperone of NMII, decreases stack length in the contractile ring in U-2 OS cells by decreasing the protein levels of NMIIA and NMIIB (i.e., a decrease in the total amount of NMII) [33]. Our isoform-specific KO experiments suggest that NMIIB functions in stack expansion because it crosslinks actin filaments and is more static in NMII filaments than NMIIA.

Membrane blebbing occurs when the plasma membrane detaches from the cortical actin cytoskeleton due to cortical contraction following NMII activation [49]. Blebbing is often observed at polar regions of dividing cells [50]. Blebs at polar regions were proposed to release pressure and thereby reduce contractile tension [51], and such polar blebbing is important for proper cytokinesis [52]. Indeed, inhibition of NMII ATPase activity by treatment with blebbistatin blocks this blebbing [34]. In this study, polar blebbing was not observed in NMIIA-KO cells (Movie S2 and Fig. S4), indicating that cortical contraction force is reduced in these cells. This is consistent with the finding that cortical stiffness was decreased in NMIIA-KO cells by AFM measurements (Fig. 6). On the other hand, polar

blebbing was observed in NMIIB-KO cells (Movie S2 and Fig. S4), in which NMIIA localized to the polar cortex (Fig. 3B). These results suggest that NMIIA plays a role not only in constriction of the contractile ring, but also in polar blebbing to ensure proper cytokinesis (Fig. 7).

The relative expression levels of NMII isoforms markedly differ between various cells and tissues [53]. We propose that the distinct functions of NMIIA and NMIIB contribute to the characteristic mechanisms underlying cytokinesis in diverse cell types. The behaviors of NMII isoforms and the effects of their KO in a variety of cell types with different expression levels of these isoforms should be investigated in the future.

Acknowledgements

We are grateful to the Nikon Imaging Center (Hokkaido University) for assistance with microscopy, image acquisition, and analysis. This work was supported by a Grant-in-Aid for Scientific Research from the Japan Society for the Promotion of Science (no. 18K0620008 to M. T.), JSPS KAKENHI Grant Number JP16H06280, a Grant-in-Aid for Scientific Research on Innovative Areas ― Platforms for Advanced Technologies and Research Resources "Advanced Bioimaging Support", and the Cooperative Research Program of the "Network Joint Research Center for Materials and Devices". This work was also supported by AMED (no. JP18gm0810007 to H. H.).

References

[1] T.D. Pollard, Mechanics of cytokinesis in eukaryotes, Curr. Opin. Cell Biol. 22 (2010) 50-56.

[2] R.A. Green, E. Paluch, K. Oegema, Cytokinesis in animal cells, Annu. Rev. Cell Dev. Biol. 28 (2012) 29-58.

[3] N. Ramkumar, B. Baum, Coupling changes in cell shape to chromosome segregation, Nat. Rev. Mol. Cell Biol. 17 (2016) 511-521.

[4] A. Basant, M. Glotzer, Spatiotemporal regulation of RhoA during cytokinesis, Curr. Biol. 28 (2018) R570-R580.

[5] M. Vicente-Manzanares, X. Ma, R.S. Adelstein, A.R. Horwitz, Non-muscle myosin II takes centre stage in cell adhesion and migration, Nat. Rev. Mol. Cell Biol. 10 (2009) 778-790.

[6] S.M. Heissler, D.J. Manstein, Nonmuscle myosin-2: mix and match, Cell. Mol. Life Sci. 70 (2013) 1-21.

[7] T. Kamasaki, M. Osumi, I. Mabuchi, Three-dimensional arrangement of F-actin in the contractile ring of fission yeast, J. Cell Biol. 178 (2007) 765-771.

[8] F. Wang, M. Kovács, A. Hu, H. Limouze, E.V. Harvey, J.R. Sellers, Kinetic mechanism of non-muscle myosin IIB: functional adaptations for tension generation and maintenance, J. Biol. Chem. 278 (2003) 27439-27448.

[9] M. Kovács, F. Wang , A. Hu, Y. Zhang, J.R. Sellers, Functional divergence of human cytoplasmic myosin II: kinetic characterization of the non-muscle IIA isoform, J. Biol. Chem. 278 (2003) 38132-38140.

[10] M.A. Conti, S. Even-Ram, C. Liu, K.M. Yamada, R.S. Adelstein, Defects in cell adhesion and the visceral endoderm following ablation of nonmuscle myosin heavy chain II-A in mice, J. Biol. Chem. 279 (2004) 41263-41266.

[11] A.N. Tullio, D. Accili, V.J. Ferrans, Z.X. Yu, K. Takeda, A. Grinberg, H. Westphal, Y.A. Preston, R.S. Adelstein, Nonmuscle myosin II-B is required for normal development of the mouseheart, Proc. Natl. Acad. Sci. USA 94 (1997)

12407-12412.
[12] C-W. Chang, S. Kumar, Nonmuscle myosin II isoforms and functional domains to stress fiber mechanics, Sci. Rep. 5 (2015) 13736.
[13] M.S. Shutova, S.B. Asokan, S. Talwar, R.K. Assoian, J.E. Bear, T.M. Svitkina, Self-sorting of nonmuscle myosins IIA and IIB polarizes the cytoskeleton and modulates cell motility, J. Cell Biol. 217 (2017) 2877-2889.
[14] M. Kuragano, T.Q.P. Uyeda, K. Kamijo, Y. Murakami, M. Takahashi, Different contributions of nonmuscle myosin IIA and IIB to the organization of stress fiber subtypes in fibroblasts, Mol. Biol. Cell 29 (2018) 911-922.
[15] M. Smutny, H.L. Cox, J.M. Leerberg, E.M. Kovacs, M.A. Conti, C. Ferguson, N.A. Hamilton, R.G. Parton, R.S. Adelstein, A.S. Yap, Myosin II isoforms identify distinct functional modules that support integrity of the epithelial zonula adherens, Nat. Cell Biol. 12 (2010) 696-702.
[16] M. Raab, J. Swift, P.C.D.P. Dingal, P. Shah, J.W. Shin, D.E. Discher, Crawling from soft to stiff matrix polarizes the cytoskeleton and phosphoregulates myosin-II heavy chain, J. Cell Biol. 199 (2012) 669-683.
[17] M. Kuragano, Y. Murakami, M. Takahashi, Nonmuscle myosin IIA and IIB differentially contribute to intrinsic and directed migration of human embryonic lung fibroblasts, Biochem. Biophys. Res. Commun. 498 (2018) 25-31.
[18] T. Kiboku, T. Katoh, A. Nakamura, A. Kitamura, M. Kinjo, Y. Murakami, M. Takahashi, Nonmuscle myosin II folds into a 10S form via two portions of tail for dynamic subcellular localization, Genes Cells 18 (2013) 90-109.
[19] T. Saitoh, S. Takemura, K. Ueda, H. Hosoya, M. Nagayama, H. Haga, K. Kawabata, A. Yamagishi, M. Takahashi, Differential localization of non-muscle myosin II isoforms and phosphorylated regulatory light chains in human MRC-5 fibroblasts, FEBS Lett. 509 (2001) 365-369.
[20] M.K. Sato, M. Takahashi, M. Yazawa, Two regions of the tail are necessary for the isoform-specific functions of nonmuscle myosin IIB, Mol. Biol. Cell 18 (2007) 1009-1017.
[21] T.G. Montague, J.M. Cruz, J.A. Gagnon, J.M. Church, E. Valen, CHOPCHOP: a CRISPR/Cas9 and TALEN web tool for genome editing, Nucleic Acid Res. 42 (2014) W401-W407.
[22] A. Nagasaki, Y. Kato, K. Meguro, A. Yamagishi, C. Nakamura, T.Q.P. Uyeda, A genome editing vector that enables easy selection and identification of knockout cells, Plasmid 98 (2018) 37-44.
[23] S. Hiruma, T. Kamasaki, K. Otomo, T. Nemoto, R. Uehara, Dynamics and function of ERM proteins during cytokinesis in human cells, FEBS Lett. 591 (2017) 3296-3309.
[24] N. Gustafsson, S. Culley, G. Ashdown, D.M. Owen, P.M. Pereira, R. Henriques, Fast live-cell conventional fluorophore nanoscopy with ImageJ through super-resolution radial fluctuations, Nat. Commun. 7 (2016)
[25] P. Maupin, C.L. Phillips, R.S. Adelstein, T.D. Pollard, Differential localization of myosin-II isozymes in human cultured cells and blood cells, J. Cell Sci. 107 (1994) 3077-3090.
[26] T. Shimozawa, K. Yamagata, T. Kondo, S. Hayashi, A. Shitamukai, D. Konno, F. Matsuzaki, J. Takayama, S. Onami, H. Nakayama, Y. Kosugi, T.M. Watanabe, K. Fujita, Y. Mimori-Kiyosue, Improving spinning disk confocal microscopy by preventing pinhole cross-talk for intravital imaging, Proc. Natl. Acad. Sci. USA 110 (2013) 3399-3404.

[27] K. Otomo, T. Hibi, T. Murata, H. Watanabe, R. Kawakami, H. Nakayama, M. Hasebe, T. Nemoto, Multi-point Scanning two-photon excitation microscopy by utilizing a high-peak-power 1042-nm Laser, Anal. Sci. 31 (2015) 307-313.

[28] M. Drobizhev, N.S. Makarov, S.E. Tillo, T.E. Hughes, A. Rebane, Two-photon absorption properties of fluorescent proteins, Nat. Methods 8 (2011) 393-399.

[29] A.B. Verkhovsky, T.M. Svitkina, G.G. Borisy, Myosin II filament assemblies in the active lamella of fibroblasts: their morphogenesis and role in the formation of actin filament bundles, J. Cell Biol. 131 (1995) 989-1002.

[30] A.M. Fenix, N. Taneja, C.A. Buttler, J. Lewis, S.B. Van Engelenburg, R. Ohi, D.T. Burnette, Expansion and concatenation of nonmuscle myosin IIA filaments drive cellular contractile system formation during interphase and mitosis, Mol. Biol. Cell 27 (2016) 1465-1478.

[31] J.R. Beach, K.S. Bruun, L. Shao, D. Li, Z. Swider, K. Remmert, Y. Zhang, M.A. Conti, R.S. Adelstein, N.M. Rusan, E. Betzig, J.A. Hammer, Actin dynamics and competition for myosin monomer govern the sequential amplification of myosin filaments, Nat. Cell Biol. 19 (2017) 85-93.

[32] S. Hu, K. Dasbiswas, Z. Guo, Y.H. Tee, V. Thiagarajan, P. Hersen, T.L. Chew, S.A. Safran, R. Zaidel-Bar, A.D. Bershadsky, Long-range self-organization of cytoskeletal myosin II filament stacks, Nat. Cell Biol. 19 (2017) 133-141.

[33] J.I. Lehtimäki, A.M. Fenix, T.M. Kotila, G. Balistreri, L. Paavolainen, M. Varjosalo, D.T. Burnette, P. Lappalainen, UNC-45a promotes myosin folding and stress fiber assembly, J. Cell Biol. 216 (2017) 4053-4072.

[34] A.F. Straight, A. Cheung, J. Limouze, I. Chen, N.J. Westwood, J.R. Sellers, T.J. Mitchison, Dissecting temporal and spatial control of cytokinesis with a myosin II inhibitor, Science 299 (2003) 1743-1747.

[35] M.P. Stewart, J. Helenius, Y. Toyoda, S.P. Ramanathan, D.J. Muller, A.A. Hyman, Hydrostatic pressure and the actomyosin cortex drive mitotic cell rounding, Nature 469 (2011) 226-230.

[36] P. Chugh, A.G. Clark, M.B. Smith, D.A.D. Cassani, K. Dierkes, A. Ragab, P.P. Roux, G. Charras, G. Salbreux, E.K. Paluch, Actin cortex architecture regulates cell surface tension, Nat. Cell Biol. 19 (2017) 689-697.

[37] V.C. Bui, T.H. Nguyen, Biophysical characteristics of hematopoietic cells during division, Exp. Cell Res. 367 (2018) 132-136.

[38] J.C. Sandquist, A.R. Means, The C-terminal tail region of nonmuscle myosin II directs isoform-specific distribution in migrating cells, Mol. Biol. Cell 19 (2008) 5156-5167.

[39] M. Vicente-Manzanares, M.A. Koach, L. Whitmore, M.L. Lamers, A.F. Horwitz, Segregation and activation of myosin IIB creates a rear in migrating cells, J. Cell Biol. 183 (2008) 543-554.

[40] T. Nakasawa, M. Takahashi, R. Matsuzawa, S. Aikawa, Y. Togashi, T. Saitoh, A. Yamagishi, M. Yazawa, Critical regions for assembly of vertebrate nonmuscle myosin II, Biochemistry 44 (2005) 174-183.

[41] N. Murakami, S.S. Singh, V.P.S. Chauhan, M. Elzinga, Phospholipid binding, phosphorylation by protein kinase C, and filament assembly of the COOH terminal heavy chain fragments of nonmuscle myosin II isoforms MIIA and MIIB, Biochemistry 34 (1995) 16046-16055.

[42] I. Badirou, J. Pan, C. Legrand, A. Wang, L. Lordier, S. Boukour, A. Roy, W. Vainchenker, Y. Chang, Carboxyl-terminal-dependent recruitment of nonmuscle myosin II to megakaryocyte contractile ring during polyploidization, Blood 124 (2014) 2564-2568.

[43] J.R. Beach, L. Shao, K. Remmert, D. Li, E. Betzig, J.A. Hammer III, Nonmuscle myosin II isoforms coassemble in living cells, Curr. Biol. 24 (2014) 1160-1166.

[44] M.S. Shutova, W.A. Spessott, C.G. Giraudo, T.M. Svitkina, Endogenous species of mammalian nonmuscle myosin IIA and IIB include activated monomer and heteropolymers, Curr. Biol. 24 (2014) 1958-1968.

[45] L. Lordier, D. Bluteau, A. Jalil, C. Legrand, J. Pan, P. Rameau, D. Jouni, O. Bluteau, T. Mercher, C. Leon, C. Gachet, N. Debili, W. Vainchenker, H. Raslova, Y. Chang, RUNX1-induced silencing of non-muscle myosin heavy chain IIB contributes to megakaryocyte polyploidization, Nat. Commun. 717 (2012).

[46] O.M. Rossier, N. Gauthier, N. Biais, W. Vonnegut, M.A. Fardin, P. Avigan, E.R. Heller, A. Mathur, S. Ghassemi, M.S. Koechert, J.C. Hone, M.P. Sheetz, Force generated by actomyosin contraction builds bridges between adhesive contacts, EMBO J. 29 (2010) 1055-1068.

[47] L. Melli, N. Billington, S.A. Sun, J.E. Bird, A. Nagy, T. B. Friedman, Y. Takagi, J.R. Sellers, Bipolar filaments of human nonmuscle myosin 2-A and 2-B have distinct motile and mechanical properties, eLife 7 (2018) e32871.

[48] K.G. Bourdages, B. Lacroix, J.F. Dorn, C.P. Descovich, A.S. Maddox, Quantitative analysis of cytokinesis in situ during C. elegans postembryonic development, PLoS One 9 (2014) e116240.

[49] G.T. Charras, J.C. Yarrow, M.A. Horton, L. Mahadevan, T.J. Mitchison, Non-equilibration of hydrostatic pressure in blebbing cells, Nature 435 (2005) 365-369.

[50] J-S. Lee, K. Kamijo, N. Ohara, T. Kitamura, T. Miki, MgcRacGAP regulates cortical through RhoA during cytokinesis, Exp. Cell Res. 293 (2004) 275-282.

[51] J-Y. Tinevez, U. Schulze, G. Salbreux, J. Roensch, J-F. Joanny, E. Paluch, Role of cortical tension in bleb growth, Proc. Natl. Acad. Sci. USA 106 (2009) 18581-18586.

[52] J. Sedzinski, M. Biro, A. Oswald, J.-Y. Tinevez, G. Salbreux, E. Paluch, Polar actomyosin contractility destabilizes the position of the cytokinetic furrow, Nature 476 (2011) 462-466.

[53] X. Ma, S.S. Jana, M.A. Conti, S. Kawamoto, W.C. Claycomb, R.S. Adelstein, Ablation of nonmuscle myosin II-B and II-C reveals a role for nonmuscle myosin II in cardiac myocyte karyokinesis, Mol. Biol. Cell 21 (2010) 3952-3962.

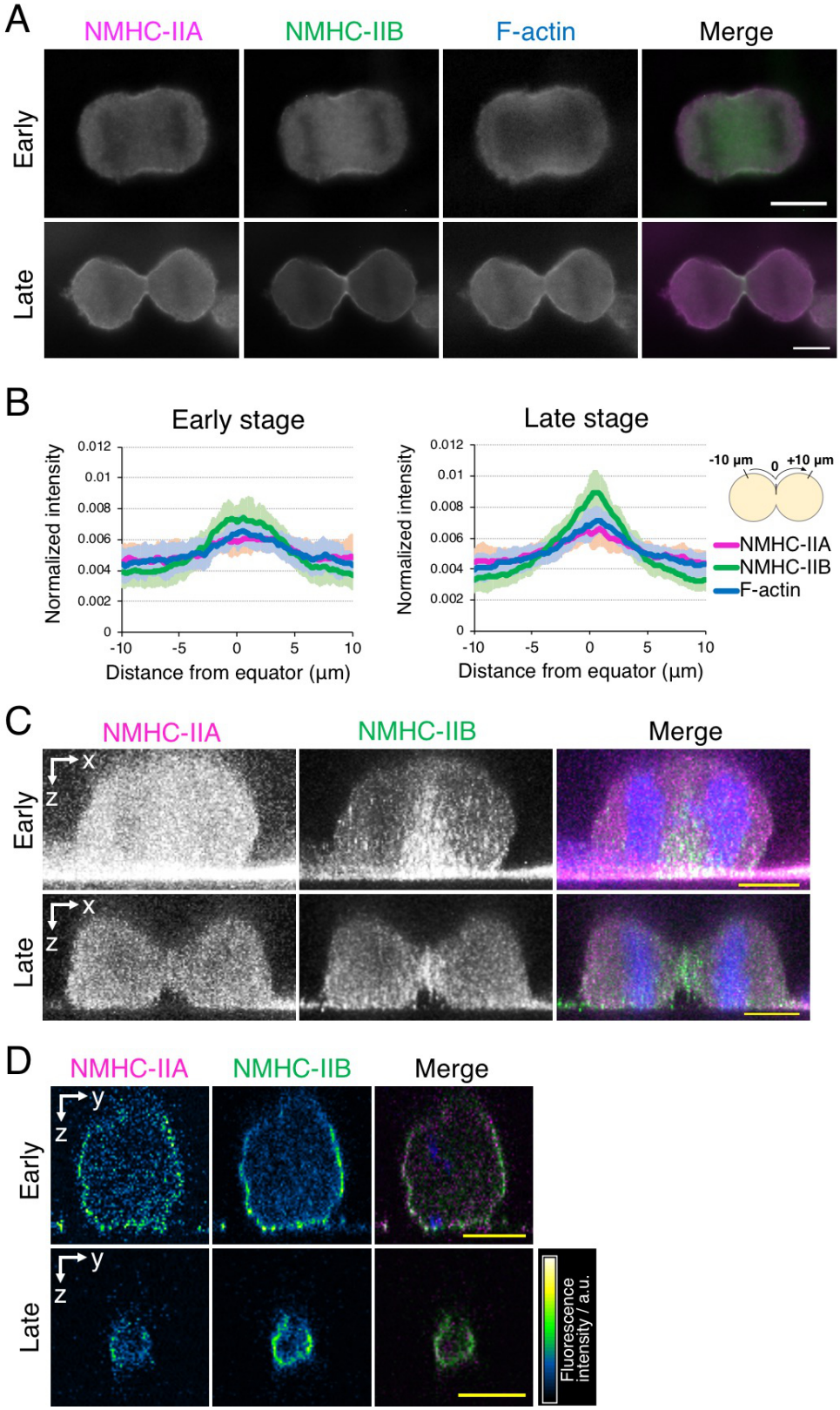

Fig. 1. Localizations of NMIIA and NMIIB during cytokinesis in human immortalized fibroblasts. (A) Representative images of direct immunofluorescence staining of endogenous NMHC-IIA and NMHC-IIB at early

(upper panels) and late (lower panels) stages of cytokinesis in VA13 cells. Filamentous actin (F-actin) was stained with Alexa Fluor 350-conjugated phalloidin. Merged images show combined NMHC-IIA and NMHC-IIB staining. Images were acquired using a conventional fluorescence microscope. Bar, 10 μm. (B) Line profiles of immunofluorescence signals along the cell cortex. Mean ± SD of 30 line profiles in 15 cells from three independent experiments. Cells with a furrow width larger and smaller than 10 μm were analyzed to investigate the early (left panel) and late (right panel) stages of cytokinesis, respectively. (C, D) Three-dimensional direct immunofluorescence staining of endogenous NMHC-IIA and NMHC-IIB in VA13 cells at early (upper panels) and late (lower panels) stages of cytokinesis. DNA was stained with DAPI. Images were acquired using a conventional confocal microscope, reconstructed from z-stacks (~20 μm thick) at 0.25 μm intervals, and visualized by maximum intensity projection. Side views (C) and cross-section views (D) of the equatorial plane. Bar, 10 μm.

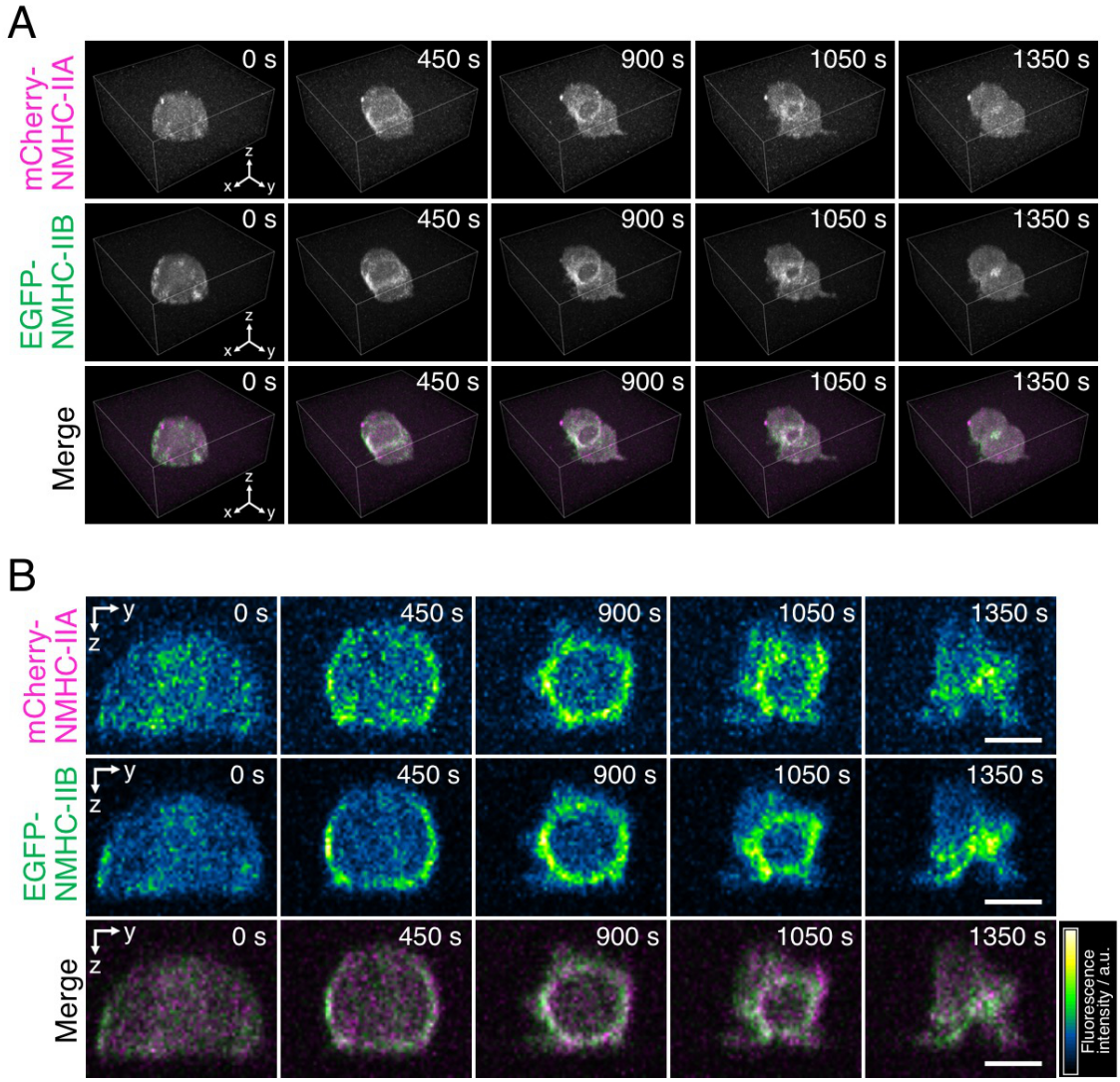

Fig. 2. Three-dimensional time-lapse imaging of cytokinesis in a VA13 cell. Images were acquired using two-photon excitation spinning-disk confocal microscopy and reconstructed from z-stacks (25 μm thick) at 0.5 μm intervals. The exposure time was 270 ms, and the three-dimensional time-lapse interval was 30 s. (A) Images showing mCherry-NMHC-IIA and EGFP-NMHC-IIB fluorescence from Movie S1 at 0, 450, 900, 1050, and 1350 s after starting time-lapse image acquisition. (B) Cross-section views of the equatorial plane reconstructed from the images shown in panel A. Bar, 10 μm.

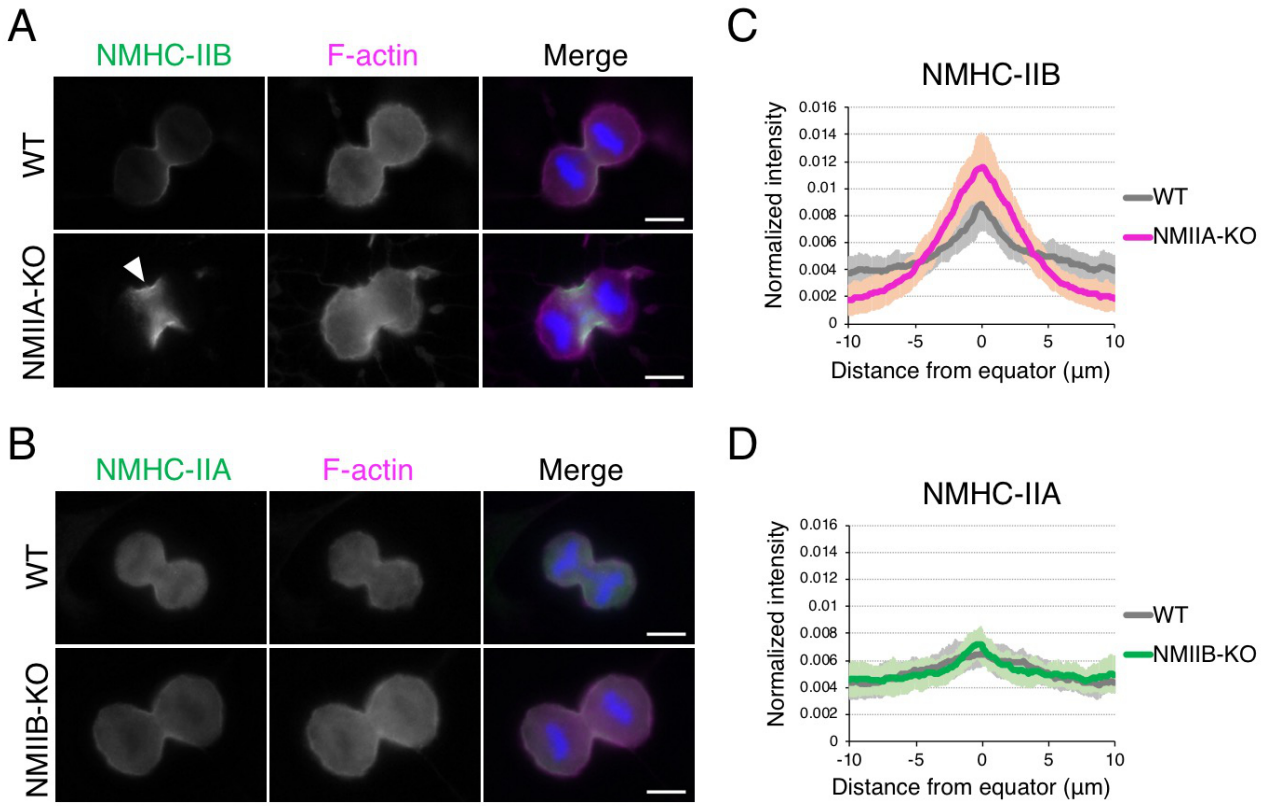

Fig. 3. Localizations of NMIIA and NMIIB during cytokinesis in NMII isoform-specific KO cells. (A, B) Representative images of indirect immunofluorescence staining of endogenous NMHC-IIB (A) and NMHC-IIA (B) during cytokinesis in WT and NMII isoform-specific KO cells. F-actin and DNA were stained with TRITC-conjugated phalloidin and DAPI, respectively. Images were acquired using a conventional fluorescence microscope. Bar, 10 μm. (C, D) Line profiles of immunofluorescence signals along the cell cortex in (A) and (B). Mean ± SD of 30 line profiles in 15 cells from three independent experiments. Cells with a furrow width less than 10 μm were analyzed. Note that NMIIB substantially localized to the cleavage furrow in NMIIA-KO cells (C, and arrowhead in A).

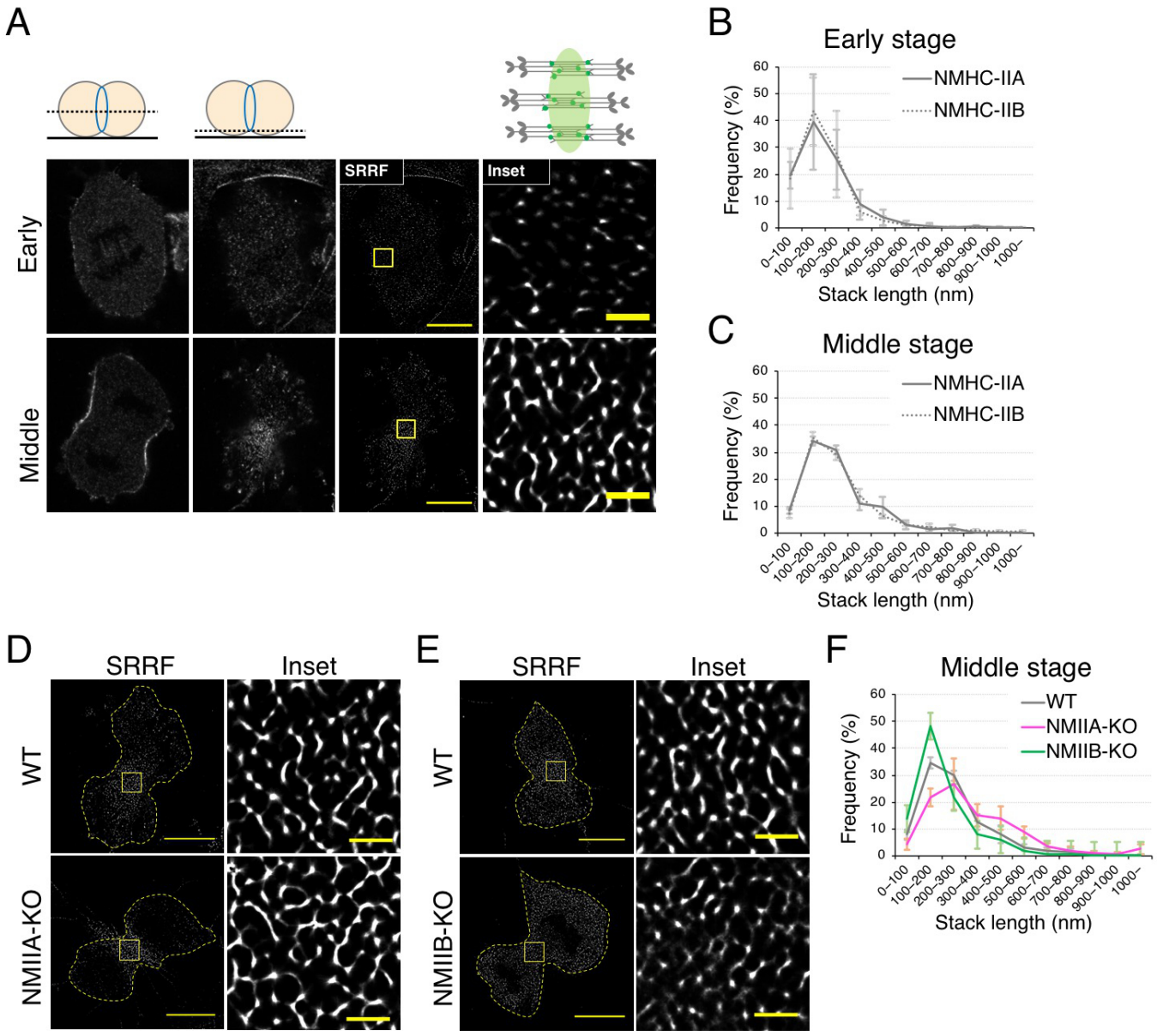

Fig. 4. Organization of NMII-F stacks in the cleavage furrow of NMIIA-KO and NMIIB-KO cells. (A) Representative images of SRRF analysis. VA13 cells were immunostained with an anti-NMHC-IIB primary antibody followed by an Alexa Fluor 488-conjugated secondary antibody. Images were acquired using a conventional confocal microscope at early (upper panels) and middle (lower panels) stages of cytokinesis. Single frames at the indicated confocal optical section corresponding to the middle plane of the cell (first column) and the very bottom of the cleavage furrow (second column) are shown. The third and fourth columns show images after SRRF reconstruction (bar, 10 μm) and expanded views of the yellow boxed regions (bar, 1 μm), respectively. Each SRRF image was reconstructed from 50 single frames. The schematic illustration above fourth column indicates the structure of a NMII-F stack. Immunofluorescence by anti-NMHC-IIs antibodies, which recognize the C-terminal tail end of NMII molecule, provides a linear fluorescent signal (indicated by light green shading). (B, C) Histograms of stack length at early (B) and middle (C) stages of cytokinesis. (D, E) Stack length was increased and decreased in NMIIA-KO cells (D, lower panels) and NMIIB-KO cells (E, lower panels), respectively. Bars are 10 and 1 μm in SRRF images

and expanded views of the yellow boxed regions, respectively. (F) Quantification of stack length in NMIIA-KO and NMIIB-KO cells. Note that stack length was increased and decreased in NMIIA-KO and NMIIB-KO cells, respectively.

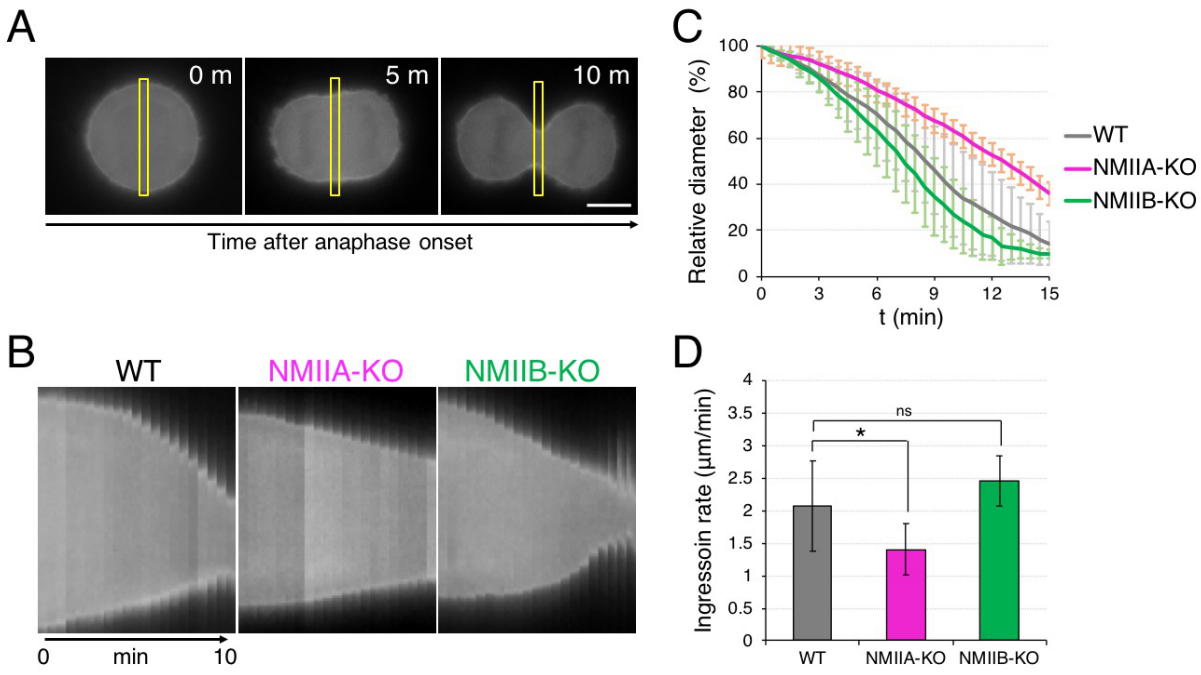

Fig. 5. Furrow ingression rates in NMIIA-KO and NMIIB-KO cells. (A) A time series of images showing furrow ingression in a WT cell expressing mApple-lifeact from Movie S2. The yellow boxes indicate the equatorial plane used to generate kymographs. Bar, 10 μm. (B) Kymographs of the equatorial plane in the indicated cell lines. Time 0 indicates anaphase onset. (C) Time courses of the furrow ingression level in the indicated cell lines. Mean ± SD of ten cells from at least three independent experiments per cell line. (D) Furrow ingression rates calculated from the data presented in panel C. *P < 0.05.

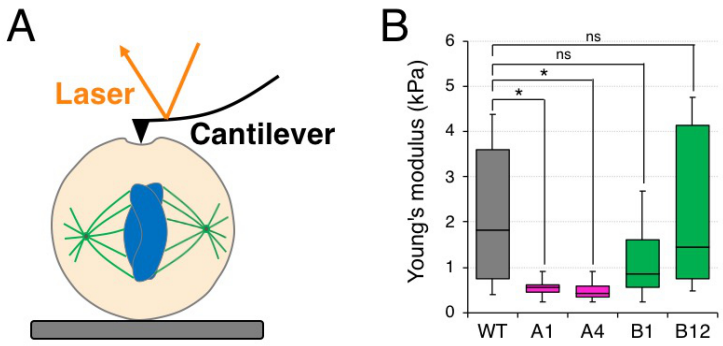

Fig. 6. Measurement of cortical stiffness in metaphase. (A) Schematic illustration of the measurement of cortical stiffness in a rounded cell by AFM. (B) Cortical stiffness in WT, NMIIA-KO (A1 and A4), and NMIIB-KO (B1 and B12) cells. n=11–15 cells from three independent experiments per cell line. *P < 0.05.

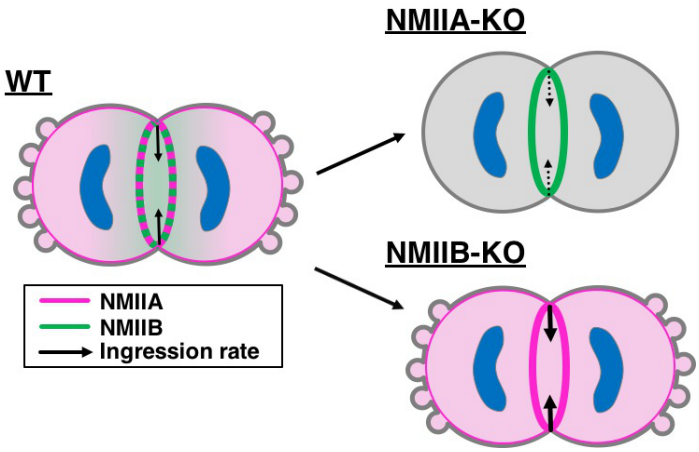

Fig. 7. A model of how NMIIA and NMIIB mechanically support proper cytokinesis. Schematic illustrations depicting the localizations of NMII isoforms and cell shape. During cytokinesis, NMIIA and NMIIB localize to the contractile ring under the control of the delicate balance of their relative expression levels (NMIIA＞NMIIB) and assembly properties (NMIIB＞NMIIA). A portion of NMIIA is diffusely distributed in the cytoplasm and localizes to the cell cortex adjacent to the contractile ring. In NMIIA-KO cells, most NMIIB accumulates in the contractile ring and the rate of furrow ingression is decreased. In NMIIB-KO cells, localization of NMIIA to the contractile ring and the rate of furrow ingression are slightly increased. Polar blebbing does not occur in NMIIA-KO cells, probably due to a lack of polar cortical tension, which is mainly generated by NMIIA.